RSC Advances

PAPER

View Article Online
View Journal | View Issue

Cite this: *RSC Adv.*, 2017, **7**, 47643

Oxygen electrode reactions of doped $BiFeO_3$ materials for low and elevated temperature fuel cell applications

Rana Arslan Afzal,†[a] Ka-Young Park,†[a] Sung-Hwa Cho,[a] Nam-In Kim,[a] Sung Ryul Choi,[a] Jung Hyun Kim,[b] Hyung-Tae Lim[c] and Jun-Young Park *[a]

Received 5th August 2017
Accepted 3rd October 2017

DOI: 10.1039/c7ra08671g

rsc.li/rsc-advances

Perovskite-based catalysts have been considered as candidate bifunctional electrocatalysts for oxygen evolution (OER) and reduction reactions (ORR) for unitized regenerative fuel cells (URFCs), because of their excellent catalytic activity and durability at low temperature. Furthermore, perovskite-structured materials can be utilized as an oxygen electrode material for solid oxide fuel cells (SOFCs) at even elevated temperatures due to their distinctive layered structure, providing great flexibility regarding the modification of their electronic configurations. Herein, we investigate whether alkaline earth metal-doped bismuth iron oxides ($Bi_{0.6}M_{0.4}FeO_3$, M = Ba, Sr, Ca, and Mg) can act as both bifunctional catalysts for URFCs and cathode materials for SOFCs. Among these, $Bi_{0.6}Ca_{0.4}FeO_3$ (BCFO) exhibits remarkable OER and ORR catalytic performances, with better long-term stability than that of a pristine $BiFeO_3$ (BFO) catalyst in alkaline media at room temperature. Moreover, the DC conductivity of BCFO is more than 2 to 3 orders of magnitude higher than that of the BFO material at 500–700 °C for SOFCs. In addition, BCFO has a α_{TEC} value of 12.4×10^{-6} K^{-1} at 25–650 °C, which is near those of yttria-stabilized zirconia and rare-earth-doped ceria electrolytes. Hence, BCFO demonstrates potential as an oxygen electrode material for operation at room and elevated temperatures.

1. Introduction

The global climate change with over-extraction of fossil fuels is bringing about the changeover from internal combustion engines to clean and sustainable renewable energy systems. In particular, electrochemical-based energy conversion and storage devices, such as fuel cells, water-splitting cells, and rechargeable metal–air batteries, are currently being investigated as sustainable energy systems with solar and wind systems.[1–5] Among these, fuel cells are the most promising alternative, due to their low emission, high-efficiency, and reasonable energy density.[6,7] The fuel cell is a clean electrochemical cell that converts the chemical energy from a hydrogen-containing fuel into electricity through electrochemical reactions with an oxidizing agent. Fuel cells are classified by the type of electrolyte and operating temperature they use.[8,9] Polymer electrolyte membrane fuel cells (PEMFCs) use polymer membranes (*e.g.* Nafion) as an electrolyte at lower temperature (<100 °C). In contrast, solid oxide fuel cells (SOFCs) use ceramic electrolytes (*e.g.* yttria-stabilized zirconia) at high operating temperature (600–1000 °C). The electrolytic cell is an electrochemical cell that when external electrical energy is applied, produces hydrogen with oxygen.[2,10–12] When electrical energy is applied to the electrodes, the ions (oxygen or proton) in the electrolyte are transported by redox reactions to an electrode with the opposite charge. Recently, integration of the two functionalities in a single electrochemical device, such as unitized regenerative fuel cells (URFCs, at <100 °C) and reversible solid oxide cells (RSOCs, at 600–1000 °C), has received great attention, due to the considerable simplification of system design, and the high power-to-weight ratio of energy conversion and storage systems.[13–16]

Until now, designing highly active, cost-efficient, and durable air-electrode materials has been an essential part of these fuel cells (and electrolytic cells), especially for oxygen reduction (ORR) and evolution reactions (OER), to overcome the sluggish reaction kinetics and large overpotential associated with the transportation of four protons/electrons.[17–20] For example, the current carbon-supported noble metal catalysts (*e.g.* Pt/C, PtRu/C, and Ir/C) are not feasible for large-scale commercialization of PEMFCs (or URFCs), due to high price and easy degradation of noble metal-based catalysts. Hence, one main goal of catalyst design for PEMFCs (and URFCs) is the development of highly active ORR and OER catalysts to replace

[a]*HMC, Department of Nanotechnology and Advanced Materials Engineering, Sejong University, Seoul 05006, Korea. E-mail: jyoung@sejong.ac.kr*

[b]*Department of Advanced Materials Science and Engineering, Hanbat National University, Daejeon, 34158, Korea*

[c]*School of Materials Science and Engineering, Changwon National University, Changwon 51140, Korea*

† Rana Arslan Afzal and Ka-Young Park contributed equally as first authors.

and/or decrease the carbon-supported noble metal catalysts. Alternatively, non-precious metal compounds and metal-free catalysts, such as transitional metal (*e.g.* Co, Fe, and Ni) complexes, chalcogenides, transition metal oxides or nitrides, and macrocycles, have been found to have some catalytic activity for the oxygen electrode reaction.[17,21–24] However, the complicated synthesis methods of catalysts are not suitable for reliable and scalable mass production. Further, relatively fast degradation of these catalysts was still observed during the accelerated stability test. Recently, several breakthroughs in activity and durability have been achieved in the field of non-precious metal catalysts. Suntivich *et al.*[25,26] and Grimaud *et al.*[27] demonstrated that the perovskite-based oxides with a general formula of ABO_3, which show excellent oxygen ion diffusion rate and surface exchange coefficient, can be utilized as potential competitors to noble-based catalysts for the oxygen electrode of URFCs, due to their excellent oxygen ion diffusion rate and surface exchange coefficient. Furthermore, oxygen deficient perovskites and brownmillerites have even surpassed the activity of state-of-the-art IrO_2 catalysts.[28–30]

Similarly, it is believed that the ORR is responsible for much of the performance loss of SOFCs with high cathodic overpolarization.[31] In particular, SOFCs that operate in an intermediate temperature (IT) range (500–700 °C) are of great interest, due to their low degradation rates, materials cost, and easier sealing.[32–36] However, with the decrease of operating temperature, the cathode overpotential increases significantly, because of the decreased values of the oxygen diffusion coefficient and oxygen surface exchange coefficient. Therefore, it is of great importance to develop high performance cathode materials for the IT–SOFCs. Currently, considerable efforts are devoted to cobalt-containing perovskite-type oxides, such as $Ba_{0.5}Sr_{0.5}Co_{0.8}Fe_{0.2}O_{3-\delta}$, $La_{0.5}Sr_{0.5}CoO_{3-\delta}$, and $NdBa_{0.5}Sr_{0.5}Co_{0.8}Fe_{0.2}O_{5+\delta}$, as some of the most promising cathodes for IT–SOFCs.[32,37–39] These catalysts exhibited higher electrocatalytic activity toward ORR, with much higher electrical conductivity than conventional $La_{0.5}Sr_{0.5}MnO_{3-\delta}$ cathodes. However, these cobalt-containing cathodes have some issues, like high cost, low phase stability, and high thermal expansion coefficients, leading to delamination of, or cracks in the cathode layer during the operation of SOFCs. Recently, many cobalt-free perovskite-type materials have been reported for the cathodes of IT–SOFCs. For example, the doped lanthanum ferrite perovskite oxides, $La_{0.8}Sr_{0.2}FeO_{3-\delta}$, $Ba_{0.5}Sr_{0.5}Zn_{0.2}Fe_{0.8}O_{3-\delta}$, and $LaBaCuFeO_{5+\delta}$, have been investigated as potential IT–SOFC cathodes.[40–42]

Herein we explore bismuth ferrite ($BiFeO_3$, BFO) as a novel cobalt-free cathode IT–SOFC, considering that ferrite-based materials exhibit a reasonable electrochemical performance.[43,44] The cathode material should possess high electrical conductivity for ORR with thermochemical compatibility for electrolyte at operating temperature.[45] Furthermore, we examine the feasibility of BFO-based materials as the catalyst of ORR and OER for PEMFCs and URFCs, since BFO is one of the most attractive heterogeneous catalysts.[46,47] The BFO-based materials are synthesized *via* a co-precipitation method, and their electrical conductivity and electrochemical performances are characterized in detail to investigate whether BFO performs well at both low (PEMFCs/URFCs) and elevated temperatures (SOFCs), expanding their practical applications. In addition, in order to improve the electrochemical performances of BFO as oxygen electrode materials, alkaline-earth metal ions (Mg^{2+}, Ca^{2+}, Sr^{2+}, and Ba^{2+}) are doped into the A-site of the Bi^{3+} ions. The doping of alkaline earth metal into BFO can result in the increment of transport rates of charge species for the electrochemical reactions through change of the electronic structure.

2. Experimental section

2.1 Preparations of BFO and doped-BFOs

The pristine- and modified-BFO catalysts were synthesized by a coprecipitation method. Stoichiometric amounts of bismuth(III) nitrate hydrate ($Bi(NO_3)_3 \cdot xH_2O$, 99.999% purity, Alfa Aesar) and iron(III) nitrate nonahydrate ($Fe(NO_3)_3 \cdot 9H_2O$, 99.99% purity, Duksan) were dissolved in distilled water with glucose monohydrate ($C_6H_{12}O_6 \cdot H_2O$, Sigma-Aldrich) and sodium bicarbonate ($NaHCO_3$, Sigma-Aldrich). During the precipitation, the solution was stirred continuously and heated at 60 °C for 18 h. Magnesium nitrate hexahydrate ($Mg(NO_3)_2 \cdot 6H_2O$, 98.0% purity, Sigma-Aldrich), calcium nitrate tetrahydrate ($Ca(NO_3)_2 \cdot 4H_2O$, 99.0% purity, Sigma-Aldrich), strontium(II) nitrate ($Sr(NO_3)_2$, 99% purity, Alfa Aesar), and barium(II) nitrate ($Ba(NO_3)_2$, 99.95% purity, Alfa Aesar) were added into BFO as an A-site dopant. The obtained materials were centrifuged, and washed several times with ethanol and distilled water to remove impurities and residues. Finally, the precipitates were dried in an electric oven at 80 °C for 12 h, and then calcined at 500 °C for 4 h.

For the cathode materials in the SOFCs, the calcined powders were ground using a mortar and pestle, and pressed uniaxially (at 18 MPa) for 1 min. The pellets were then sintered at 700 °C for 4 h, with heating and cooling rates of 5 °C min^{-1}.

2.2 Characterizations of BFO-based materials

The crystalline phase of all samples was examined by X-ray diffraction (XRD, D/MAX 2500, Rigaku) with Cu-Kα radiation in the range of 20–80° with 0.02° step size. Rietveld refinements were performed by Fullprof software to reveal the lattice parameters and crystal structure. The morphology and microstructure of the synthesized catalysts were observed by field emission-scanning electron microscopy (FE-SEM, S-4700, Hitachi High Tech) with energy dispersive X-ray spectroscopy (EDX, Oxford Instruments) to analyze the material composition. The specific surface area of catalysts was analyzed by performing nitrogen sorption measurement at 77 K on a 3Flex surface characterization analyzer (Micromeritics, USA). The surface area was estimated using the Brunauer–Emmett–Teller (BET) equation, using 3Flex software. Pore size distributions were calculated using the Barrett–Joyner–Halenda (BJH) method from the adsorption branch of the isotherm. The X-ray photoelectron spectroscopy (XPS) was performed by spectrometer (theta probe angle-resolved XPS system, Thermo Fisher Scientific) with a monochromatized Al Kα (1486.6 eV) as X-ray source.

The chamber was kept as a vacuum condition, 1×10^{-10} Torr, and the measured data were calibrated using C 1s peak (284.6 eV) as reference. The thermal expansion coefficient (TEC) of the sintered BFO-based sample was measured using a dilatometer (Tesatronic TT-80) between room temperature and 650 °C with a heating/cooling rate of 5 °C min^{-1} in air atmosphere. The average TECs were found from the linear section of dilatometric data.

2.3 Electrochemical analysis of BFO-based catalysts

Catalyst suspensions were prepared from 10 mg of BFO-based catalyst, 5 mg carbon black (Vulcan XC-72R, Cabot), 5 wt% Nafion solution (Sigma-Aldrich), isopropanol (Daejung), and deionized (DI) water; they were then ultrasonicated for 30 min to make the homogeneous solution. The slurry was pipetted onto the glassy carbon by a microsyringe (Daihan Sci.), then heated at 60 °C to dry. 0.1 M potassium hydroxide (KOH) solution was used as electrolyte. Electrochemical measurements were carried out by rotating disk electrode (RDE) system (RRDE-3A, ALS) with galvanostat/potentiostat electrochemical analyzer (SP-150, Bio-Logic). In the three-electrode system, Hg/HgO (sat. NaOH), Pt wire, and catalyst coated-glassy carbon were applied as reference, counter, and working electrode, respectively. The measured potentials were converted to the reversible hydrogen electrode (RHE) scale according to the following relation;

$$V\,(vs.\ \mathrm{RHE}) = V\,(vs.\ \mathrm{Hg/HgO}) + 0.098 + 0.059\mathrm{pH} \quad (1)$$

The measured potentials were also compensated as 85% by *iR*-correction method. Pre-conditioning of the materials was conducted by cyclic voltammetry (CV) technique to clean the surface of the materials in N_2-saturated 0.1 M KOH solution between 0.05 and 1.2 V for 50 cycles at a scan rate of 100 mV s^{-1}. Linear sweep voltammetry (LSV) was performed to evaluate the OER and ORR performances, using the RDE from 1.2 to 1.7 V (OER) and 1.1 to 0.2 V (ORR) at a scan rate of 5 mV s^{-1} and a rotation of 1600 rpm in 0.1 M KOH solution. 20 wt% of Ir/C (Premetek) and Pt/C (Johnson Matthey) were used as reference catalysts for OER and ORR, respectively. The accelerated durability tests (ADTs) were carried out for OER (1.2–1.7 V) and ORR (0.6–1.2 V) potential ranges, respectively, at a scan rate of 200 mV s^{-1} for 1500 cycles in electrolyte solution with rotation.

For four-probe DC conductivity measurements, the sintered BFO and BCFO pellets were ground into rectangular-type bars. Four platinum wires were bound to each sample to form four contacts and leads for DC four-probe measurements. The electrical conductivity of the samples was measured by using a potentiostat/galvanostat instrument (SP-240, Biologic). By passing current and recording the voltage of the samples, four-probe DC conductivity was performed as a function of temperature in ambient air atmosphere.

3. Results and discussion

3.1 Characterizations of the doped-BFOs

Fig. 1 shows the XRD patterns of calcined pristine and alkaline earth metal oxide (MgO, CaO, SrO, and BaO)-doped $BiFeO_3$ (BFO) powders at 500 °C. In all cases, the major phases are consistent with a rhombohedral phase corresponding to the crystalline structure of trigonal BFO (JCPDS #72-2035).[48,49] Peaks that relate to the impurity ($Bi_2Fe_4O_9$) are observed at 28° and 30°, as marked with the symbol in Fig. 1(a), apart from the perovskite phase. However, the main diffraction peaks of (010), (110), (111), (020), (120), and (121) are sharp, indicating that alkaline earth metal dopants did not destroy the original lattice structure of BFO. Furthermore, it could be reasonably assumed that such a small amount of doping did not appear to influence the electrochemical performance. The average crystallite sizes of the materials were calculated by Scherrer equation (Table 1). BFO showed a larger crystallite size of 4.99 nm, compared to that of the doped BFO materials. $Bi_{0.6}Ba_{0.4}FeO_3$ (BBFO), $Bi_{0.6}Sr_{0.4}FeO_3$

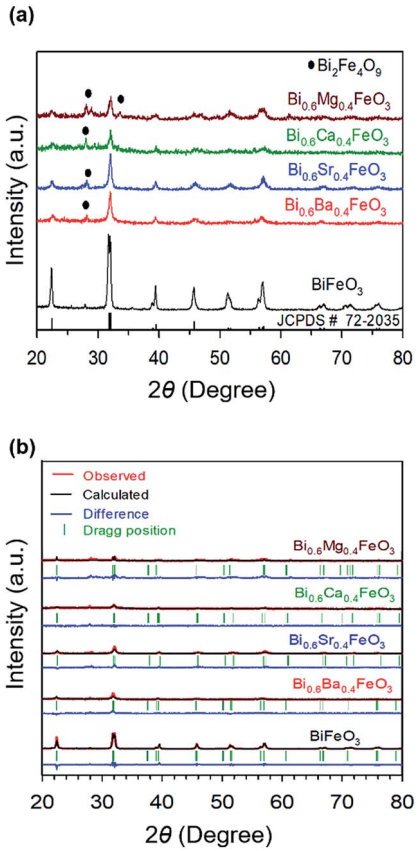

Fig. 1 (a) XRD patterns of calcined pristine and alkaline earth metal oxide (MgO, CaO, SrO, and BaO)-doped $BiFeO_3$ (BFO) powders at 500 °C, with (b) their Rietveld refinement results.

Table 1 Crystal-structural parameters of the BFO-based catalysts from Rietveld refinement

Catalyst	*a*-axis (Å)	*b*-axis (Å)	*c*-axis (Å)	Chi^2 (χ^2)	Crystallite size (nm)
$BiFeO_3$	5.580	5.580	13.862	0.71	4.99
$Bi_{0.6}Ba_{0.4}FeO_3$	5.591	5.591	13.771	2.60	3.63
$Bi_{0.6}Sr_{0.4}FeO_3$	5.608	5.608	13.830	1.93	3.56
$Bi_{0.6}Ca_{0.4}FeO_3$	5.578	5.578	13.727	1.46	3.78
$Bi_{0.6}Mg_{0.4}FeO_3$	5.585	5.585	13.849	3.76	3.66

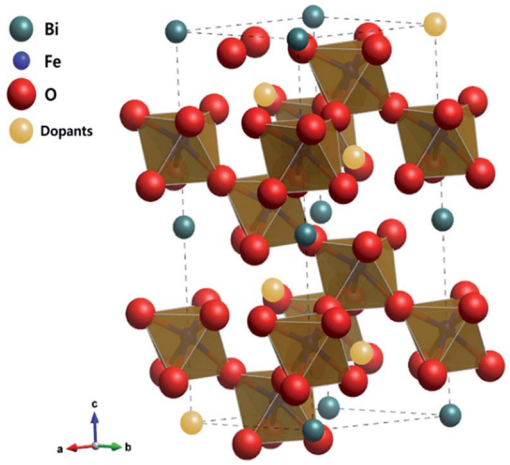

Fig. 2 Crystalline structure of alkaline earth metal oxide-doped BFO simulated by the Rietveld refinement.

(BSFO), $Bi_{0.6}Ca_{0.4}FeO_3$ (BCFO), and $Bi_{0.6}Mg_{0.4}FeO_3$ (BMFO) exhibited 3.63, 3.56, 3.78, and 3.66 nm of crystallite size, respectively, indicating that doping of alkaline earth metal contributed to decrease of the crystallite size of the BFO.[21,50]

To better understand the nature of the detailed structural information of BFO-based materials, the XRD patterns of overall catalysts were further analyzed by the Rietveld refinement using the Fullprof program,[51] and Fig. 1(b) shows the refinement results. The diffraction peaks of all samples were indexed as a rhombohedral perovskite structure with space group of *R*3*cH*, in agreement with the previous results.[49,52] Fig. 2 shows that the

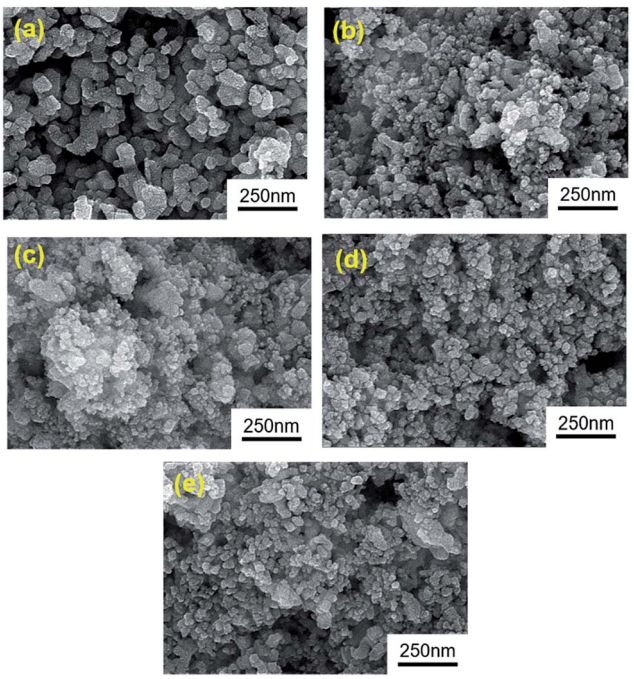

Fig. 3 Morphology and microstructure of the BFO-based catalysts examined by FE-SEM; (a) $BiFeO_3$, (b) $Bi_{0.6}Ba_{0.4}FeO_3$, (c) $Bi_{0.6}Sr_{0.4}FeO_3$, (d), $Bi_{0.6}Ca_{0.4}FeO_3$, and (e) $Bi_{0.6}Mg_{0.4}FeO_3$.

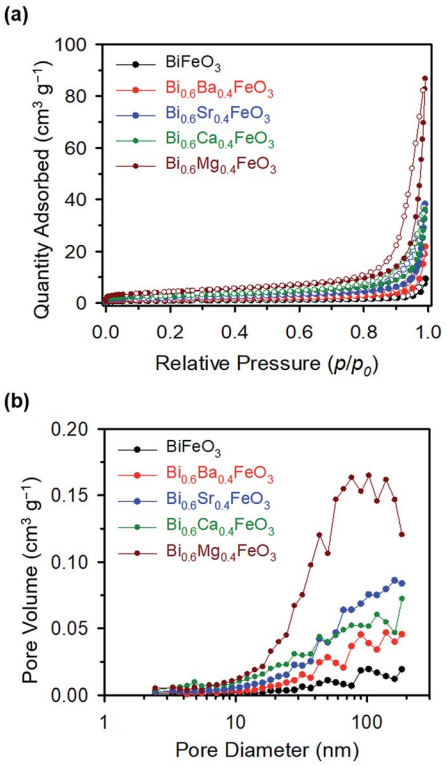

Fig. 4 (a) Nitrogen adsorption–desorption isotherms, and (b) total pore volume and pore size, obtained from adsorption branches of the BFO-based catalysts.

unit cell can be described in a hexagonal frame of reference, with the hexagonal *c*-axis parallel to the diagonals of the perovskite cube ($[111]_{pseudocubic} \parallel [001]_{hexagonal}$). The average hexagonal lattice parameters are $a_{hex} = 5.59$ Å and $c_{hex} = 13.80$ Å, and Table 1 shows the refinement parameters of BFO materials.

The chi-square (χ^2) values of BFO-based materials are reasonably low ($\chi_{BFO}^2 = 0.703$, $\chi_{BBFO}^2 = 2.60$, $\chi_{BSFO}^2 = 1.93$, $\chi_{BCFO}^2 = 1.46$, and $\chi_{BMFO}^2 = 3.76$), as the criteria for judging the quality of the profile fit. It is clear that the alkaline earth metals are doped into the A-site of the Bi^{3+} to maintain the structural stability in the ABO_3 structure (considering the tolerance factor of perovskite, $t = (\gamma_A + \gamma_O)/\sqrt{2}(\gamma_B + \gamma_O)$), since there is a large difference in ionic radii between A and B cations. Furthermore, the valence of B cations should be varied by oxygen vacancies to maintain the electroneutrality of the unit cell, because the B cations is surrounded by octahedron of oxygen anions.[53,54] In contrast, the alkaline earth metals are non-magnetic materials with a fixed ionic valence as M^{2+} (*e.g.* Mg^{2+}, Ca^{2+}, Sr^{2+}, and Ba^{2+}). The morphology and microstructure of the BFO catalysts were examined by FE-SEM. Fig. 3 shows that the BFO-containing catalysts displayed a cotton ball-like structure with agglomerated features, typical of the morphology of coprecipitated ceramic powders after calcination. The doping strategy effectively reduced the average particle size of the BFO from 84 to 40 nm, due to the interaction between dopants and surfaces (or grain boundaries), which reduces the interfacial energy at those regions.[55] This trend was in agreement with the BET results of

Table 2 Characterization data of BFO-based catalysts from N_2 adsorption–desorption isotherms

Catalyst	BET ($m^2\ g^{-1}$)	Total pore volume [$p/p_0 = 0.990$] ($cm^3\ g^{-1}$)	Mean pore diameter (nm)
$BiFeO_3$	2.8	0.012	17.4
$Bi_{0.6}Ba_{0.4}FeO_3$	4.8	0.031	25.7
$Bi_{0.6}Sr_{0.4}FeO_3$	7.4	0.056	30.7
$Bi_{0.6}Ca_{0.4}FeO_3$	9.4	0.053	22.5
$Bi_{0.6}Mg_{0.4}FeO_3$	15.1	0.130	34.6

catalysts. The BET surface area of catalysts was analyzed by nitrogen adsorption–desorption isotherms as shown in Fig. 4(a), and was determined to be 2.8, 4.8, 7.4, 9.4, and 15.1 $m^2\ g^{-1}$ for the BFO, BBFO, BSFO, BCFO, and BMFO, respectively. That is, the doping of alkaline earth metal into BFO effectively increased the surface area of the catalysts. Fig. 4(b) shows the total pore volume and pore size, which were obtained from the adsorption branches by using the BJH method. The formed pore volume and diameter of the pristine BFO were also increased by the addition of alkaline earth metal, and the mean pore diameter was 17.4, 25.7, 30.7, 22.5, and 34.6 nm for the BFO, BBFO, BSFO, BCFO, and BMFO, respectively. Table 2 lists all of the detailed data for the BET surface area, pore size, and pore volume of the BFO-based catalysts.

3.2 Electrocatalytic activity and stability of the BFO-based catalysts for OER and ORR at room temperature

The electrocatalytic activity of the BFO-based catalysts was investigated with the Hg/HgO reference electrode using RRDE measurements in an O_2-saturated 0.1 M KOH solution at a rotation speed of 1600 rpm. BFO-based particles were mixed with carbon black for the ORR activity measurements, to overcome the electronic conductivity limitations. Fig. 5(a) shows the ORR polarization curves of the catalysts.

The electrochemical performances of carbon black, Pt/C (20 wt% Pt, Johnson Matthey), and Ir/C (20 wt%, Premetek) were measured and plotted for comparison purpose. It is clearly observed that doping of alkaline earth metal into BFO makes a remarkable improvement to the ORR activity. In particular, Ca-doped BFO (BCFO) shows the best catalytic behavior for ORR among these catalysts. The onset (η_{onset}) and half-wave potential ($\eta_{half\text{-}wave}$ at -3 mA cm^{-2}) of BCFO are 0.705 and 0.619 V, respectively, as the crucial parameter to determine the level of intrinsic ORR activity, while those of BFO are 0.633 and 0.480 V. The kinetics of the BFO-based catalysts were investigated from their Tafel plots using the Tafel equation ($\eta = a + b \log j$, where η and j are the overpotential and current density, respectively) in Fig. 5(b). The measured Tafel slopes of BFO, BBFO, BSFO, BCFO, and BMFO catalysts are -99, -88, -92, -76, and -96 mV dec^{-1}, respectively. Moreover, the doped BFO materials show an increment in the exchange current density (j_0) from 3.23×10^{-9} (pristine BFO) to 5.17×10^{-8} mA cm^{-2} (BCFO). Table 3 shows the values of the ORR polarization curves.

The oxygen evolution activities of pristine and doped BFOs were also measured in a 0.1 M KOH solution at room temperature by rotating disk electrode (RDE) system. Fig. 5(c) demonstrates the linear sweep voltammetry (LSV) curves from 1.3 to 1.7 V *vs.* RHE at a scan rate of 5 mV s^{-1} to minimize the capacitive current. It is evident that the BCFO is the most highly active for the OER, compared to those of BFO, BBFO, BSFO, and

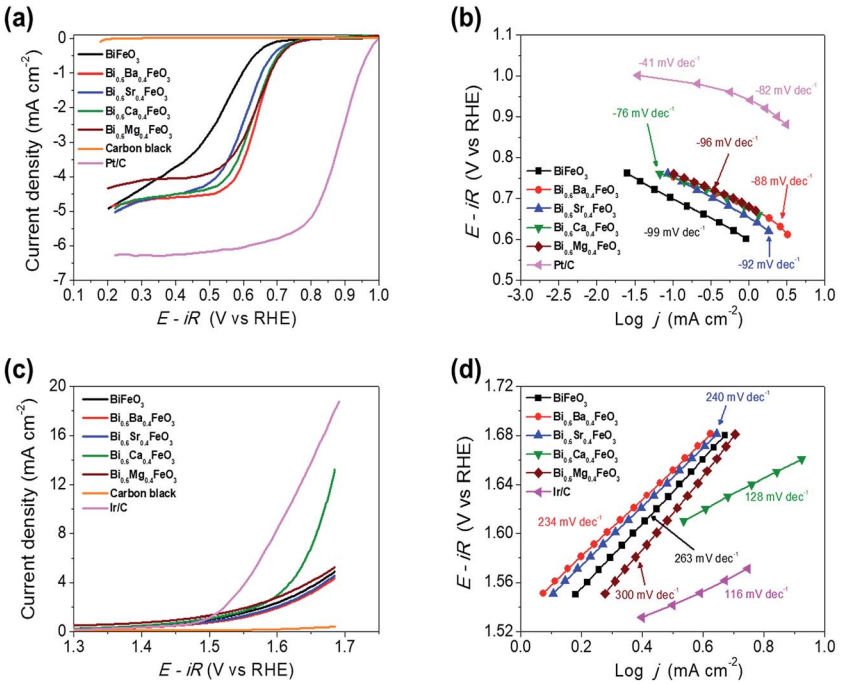

Fig. 5 Electrochemical performances of BFO-based catalysts. (a) ORR polarization curves (b) corresponding Tafel plots, (c) OER polarization curves and (d) corresponding Tafel plots of the BFO-based catalysts.

Table 3 Comparison of OER and ORR activity data for the pure $BiFeO_3$ and doped $BiFeO_3$ materials

Catalysts	ORR				OER			
	ORR onset potential, η_{onset}	E_{ORR}/V (at $j = -3$ mA cm^{-2})	Tafel slope/mV dec^{-1}	Exchange current density/mA cm^{-2}	OER onset potential, η_{onset}	j_{OER}/mA cm^{-2} (at 1.65 V)	Tafel slope/mV dec^{-1}	Exchange current density/mA cm^{-2}
$BiFeO_3$	0.633	0.480	−99	3.23×10^{-9}	1.606	3.63	263	9.24×10^{-2}
$Bi_{0.6}Ba_{0.4}FeO_3$	0.685	0.578	−88	1.77×10^{-9}	1.619	3.06	234	5.02×10^{-2}
$Bi_{0.6}Sr_{0.4}FeO_3$	0.702	0.605	−92	2.81×10^{-9}	1.618	3.29	240	5.88×10^{-2}
$Bi_{0.6}Ca_{0.4}FeO_3$	0.705	0.619	−76	5.17×10^{-8}	1.609	6.93	128	3.24×10^{-1}
$Bi_{0.6}Mg_{0.4}FeO_3$	0.708	0.593	−96	1.33×10^{-9}	1.619	4.04	300	1.63×10^{-1}

BMFO catalysts. The current density for OER (j_{OER}) of BCFO shows a significantly high value of 6.93 mA cm^{-2}, at a fixed overpotential of 0.42 V (1.65 V *vs.* RHE), which is approximately 2 times higher than that of the other catalysts. Fig. 5(d) also shows corresponding Tafel plots for OER, and the catalysts showed Tafel slopes ranging from 128 to 300 mV dec^{-1}. The BCFO catalyst exhibits the lowest Tafel slope of 128 mV dec^{-1} with high j_0 (3.24×10^{-1} mA cm^{-2}), while BFO shows 263 mV dec^{-1} and 9.24×10^{-2} mA cm^{-2} for OER. Detailed electrochemical parameters of the BFO catalysts were tabulated in Table 3.

In order to grasp the pathway for ORR, the Koutecky–Levich (K–L) plots of the BFOs materials are obtained from ORR polarization curves. The kinetic parameters can be determined by the following Koutecky–Levich equations;[56–59]

$$1/j = 1/j_L + 1/j_K = 1/(B\omega^{1/2}) + 1/j_K \quad (2)$$

$$B = 0.62nFC_0(D_0)^{3/2}\nu^{-1/6} \quad (3)$$

$$j_K = nFkC_0 \quad (4)$$

where j is the measured current density, j_L and j_K are the diffusion-limiting and kinetic current density, ω is the angular velocity of the rotating disk (rad s^{-1}), n is the number of electrons in ORR, F is Faraday constant (96 485C mol^{-1}), C_0 and D_0 are the saturation concentration (1.26×10^{-6} mol cm^{-3}) and diffusion coefficient (1.93×10^{-5} cm^2 s^{-1}) of oxygen gas, respectively, ν is the kinematic viscosity of the electrolyte (0.1 M KOH, 1.09×10^{-2} cm^2 s^{-1}), and k is the electron transfer rate constant, respectively. The K–L plots shows a linear shape in Fig. 6 and the number of electrons (n) are calculated from their slopes as 2.6 (BFO), 3.4 (BMFO), 3.5 (BBFO and BSFO), 3.7 (BCFO) at 0.5 V, respectively, indicating that the dopants (Ba, Sr, Ca, and Mg) contribute to significantly improve the intrinsic ORR activity of BFO. This result may be due to the enhanced oxygen catalytic activity through modification of the electrical properties of catalysts by doping of alkaline earth metal oxides.

In order to ascertain the chemical state (electronic state) for the individual elements, the XPS spectra are carried out (Fig. 7). It is observed that the spectra of Bi 4f and Fe 2p are almost similar for all BFO-based materials. The peaks in O 1s spectra at 530.4 and 529.15 eV are associated with the Bi_2–$(O\ 1s)_3$ and Fe_2–$(O\ 1s)_3$ bonds, respectively.[60,61] The Bi_2–$(O\ 1s)_3$ peaks were shifted in BBFO and BSFO to higher binding energy, while to lower binding energy in BMFO. This indicates that the binding energy between Bi and lattice oxygen can be varied by the dopant ions (that is, higher binding energy for larger ions and lower for smaller ions). Ca-doped BFO shows negligible change in the O 1s spectra due to the similar ionic size of Bi^{3+} and Ca^{2+} (Bi^{3+} = 1.17 Å, Ca^{2+} = 1.14 Å), which is consistent with the results of previous studies.[62–64] That is, small difference of ionic radii between Bi^{3+} and Ca^{2+} decreases the crystallite size with structural stability including the improved ORR and OER activities.[65–67] The excellent performance of BCFO for OER and ORR is also due to the rapid charge-transport property of the BCFO catalyst. The doping of CaO into BFO can result in the

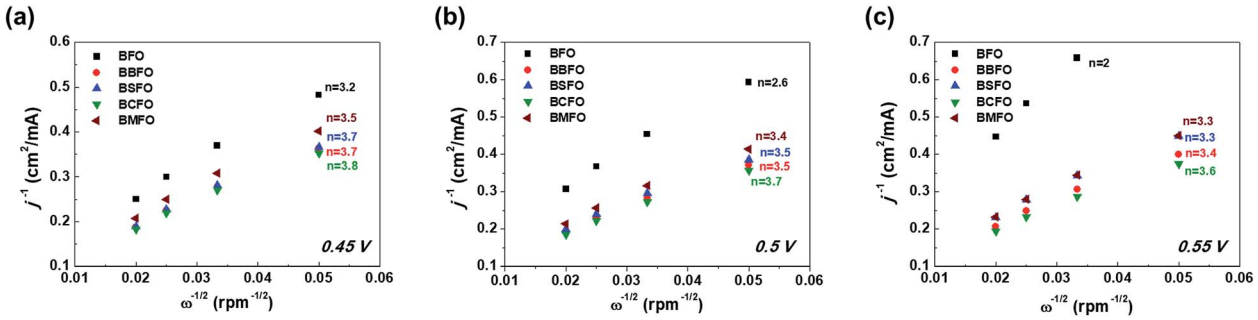

Fig. 6 Koutecky–Levich plots of alkaline earth metal-doped BFOs with the number of electrons at various ORR potentials; (a) 0.45 V, (b) 0.5 V, and (c) 0.55 V.

increment of transport rates of charge species for the electrochemical reactions through the change of electronic structure. In order to confirm this explanation, electrochemical impedance spectroscopy (EIS) was performed in a 0.1 M KOH electrolyte at room temperature. Fig. 8(a) shows the complex-plane Nyquist plots of the BFO-based catalyst at a potential of 1.65 V *vs.* RHE. The charge transfer (R_{ct}, as determined from the diameter of the semicircle of the Nyquist plot at a high frequency region) and mass transfer resistances (R_{mt}, at a low frequency region) were obtained from the fitted equivalent circuit using EC-Lab software, and are shown in Fig. 8(b). It is clear that the doping of CaO resulted in significant decrease of the R_{ct} of the BFO. R_{ct} of the BCFO decreased from 0.73 (BFO) to 0.61 ohm cm^2 (BCFO), while the R_{mt} showed negligible change. This finding is concordant with the results of the oxygen activities (OER and ORR) of the BFO-based catalysts presented in Fig. 5. Ineffective change of R_{ct} of the BBFO, BSFO, and BMFO with oxygen activity needs to more understanding as future works.

Fig. 9 shows the effect of CaO content of the BFO on the oxygen activity. The performances of Ca-doped BFO displayed with Pt/C and Ir/C for ORR and OER, respectively. In Fig. 9(a), the ORR activity of BCFO catalysts was investigated in a 0.1 M KOH solution at a rotation speed of 1600 rpm (RRDE). With increasing CaO content at room temperature, the ORR activity (in $\eta_{half\text{-}wave}$ at -3 mA cm^{-2}) increased until 40 mol%. Further increases in the CaO content resulted in decreased ORR activity of the BCFO catalysts. The $\eta_{half\text{-}wave}$ of BCFO was 0.610, 0.611, 0.616, 0.619, and 0.616 V for 10, 20, 30, 40, and 50 mol% CaO doping, respectively. For the OER activity, 40 mol% CaO doped BFO showed the lowest overpotential at a fixed current density of 5 mA cm^{-2}, as shown in the LSV curves of Fig. 9(b). The j_{OER} of BCFO was 5.09, 5.58, 5.19, 6.92, and 4.22 mA cm^{-2}, at a fixed overpotential of 0.42 V (1.65 V *vs.* RHE).

For sustainable use for bifunctional OER and ORR catalysts, long-term stability is one of the important factor.[21,47,68] The durability of BFO and BCFO was examined by the potential cycling method from 1.25 to 1.65 V (for OER) and 0.6 to 1.0 V (for ORR) for 1500 cycles in 0.1 M KOH solution. Fig. 10(a) shows the polarization curves of the OER stability tests for BFO and BCFO. After potential cycling, the OER activities of BCFO decreased from 6.98 to 5.22 mA cm^{-2} at 1.65 V, resulting in a 24% loss of

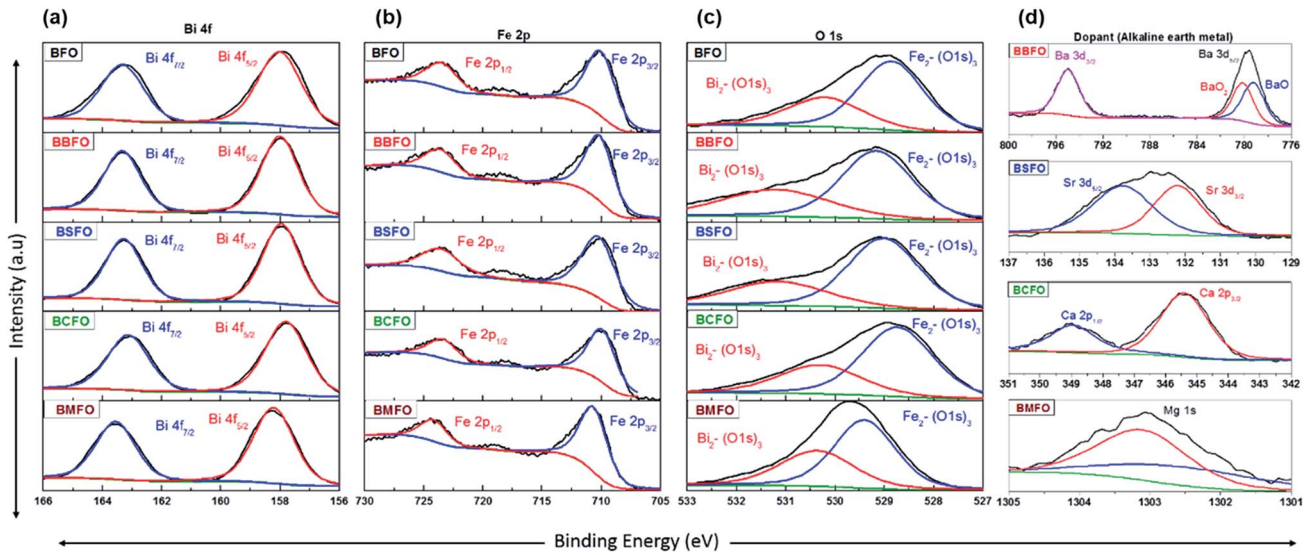

Fig. 7 XPS spectra of BFO-based catalysts. (a) Bi 4f, (b) Fe 2p, (c) O 1s, and (d) dopants (Ba 3d, Sr 3d, Ca 2p, and Mg 1s).

activity; whereas, BFO underwent a more severe degradation of 95.1% (from 3.57 to 0.172 mA cm^{-2}) (Fig. 10(a) and (c)). Fig. 10(b) and (c) show the ORR polarization curves of BFO and BCFO before and after potential cycling, and in comparison with that of the BFO catalyst. The potential decrease for ORR clearly reveals that the durability of BCFO is greater than that of the BFO. The potential of the BCFO decreased 20 mV at $\eta_{\text{half-wave}}$, whereas that of BFO decreased substantially by 34 mV after 1500 cycles. The better durability of BCFO for bifunctional oxygen reactions was mainly due to the robust crystal structure of BCFO by doped Ca^{2+} ions, which could inhibit the agglomeration and amorphization of particles during the water oxidation and reduction reactions. Many researchers reported that the surface oxidation and amorphization of oxide and agglomeration of nanoparticles are responsible as the main degradation mechanisms of OER and ORR activities during the long-term electrochemical reactions associated with oxygen.[21,51,69–71]

3.3 Thermomechanical and electrical properties of BFO and BCFO at high temperature

A major technical challenge in SOFC research is to develop cathode materials of similar thermal expansion coefficient (TEC) to those of other cell components (anode, electrolyte, and contact functional layers) to mitigate thermomechanical stresses, especially during thermal cycling.[7,39,72–75] The TEC (α_{TEC}) commonly describes how a compound changes unit cell parameter in response to temperature, and is defined as;

$$\alpha_{\text{TEC}} = \frac{1}{L_o}\frac{\Delta L_k - \Delta L_o}{T_k - T_o} \quad (5)$$

where L_o, ΔL_o, and ΔL_k are the length of the specimen at T_o (room temperature), the change in length at T_o, and the corresponding length change at temperature T_k. Fig. 11 shows the dilatometric measurement results of sintered BCFO ceramics. The typical linear thermal expansions ($\Delta L/L_o$) can be observed without any phase transformation for BCFO samples in the temperature range of room temperature to 650 °C. BCFO has a α_{TEC} value of 12.4×10^{-6} K^{-1} at between room temperature and 650 °C, and this value is very near those of the conventionally used yttria-stabilized zirconia (YSZ) ($\alpha_{\text{TEC}} \approx 11.0 \times 10^{-6}$ K^{-1}) and rare-earth-doped ceria (CeO_2) electrolytes ($\alpha_{\text{TEC}} \approx 11.9$–$13.5 \times 10^{-6}$ K^{-1}).[76–79]

Therefore, it would be beneficial to use BCFO as a cathode material with conventional electrolytes for IT–SOFCs, because cracking and delamination of the cell can be greatly reduced at high operating temperatures, through the relieving of thermal stress at the interface.

The electrical properties of the BFO and BCFO compounds were studied by four-probe DC technique between 500 and 700 °C. Fig. 12 compares the total conductivity of the BFO and BCFO cathodes in air conditions. The DC conductivity data of the BCFO were more than 2–3 orders of magnitude higher than that of the BFO material in all the measured temperature range (particularly at intermediate temperature). This indicates that the doping of CaO contributes to significantly increase of the conductivity of BFO, in agreement with the results of ORR and

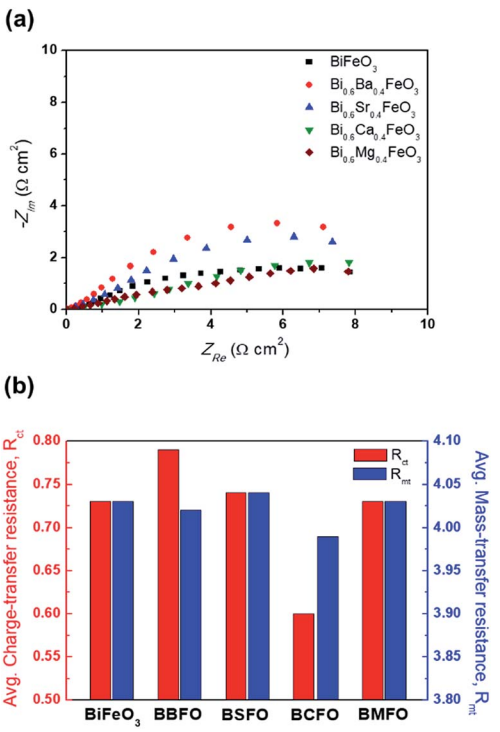

Fig. 8 (a) Complex-plane Nyquist electrochemical impedance plots, and (b) the charge transfer resistance (R_{ct}) and mass transfer resistance (R_{mt}) of catalysts in a 0.1 M KOH electrolyte at the potential of 1.65 V *vs.* RHE.

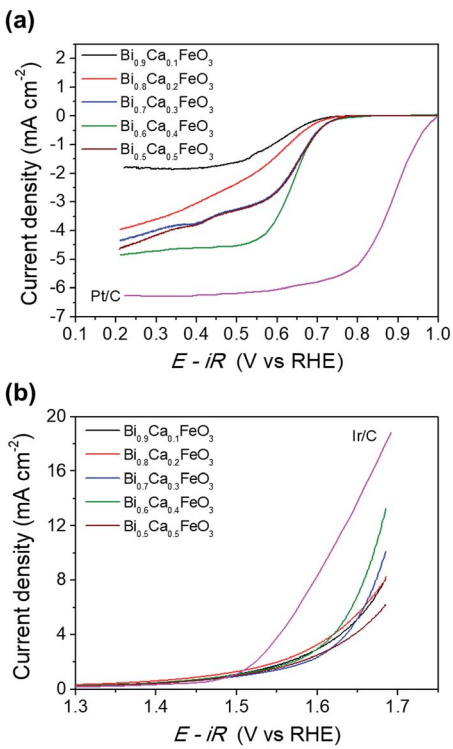

Fig. 9 (a) ORR polarization curves and (b) OER polarization curves of the $Bi_{1-x}Ca_xFeO_3$ (x = 0.1, 0.2, 0.3, 0.4, and 0.5).

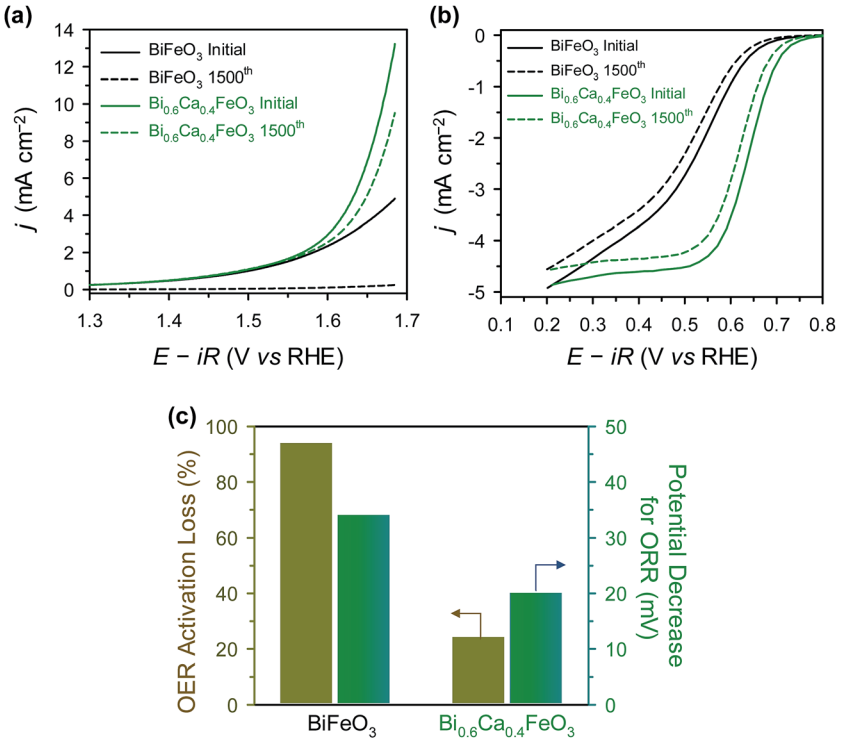

Fig. 10 (a) ORR, and (b) OER polarization curves of BFO and BCFO catalysts before (solid line), and after (dotted line), potential cycling. (c) ORR potential decrease at −3 mA cm^{-2}, and OER activity losses at 1.65 V (*vs.* RHE) of catalysts after potential cycling.

OER at room temperature. In addition, the conductivity of BCFO increased with increase of operation temperature, indicating the semiconducting behavior of BCFO. In order to examine the long-term stability of materials, the electrical conductivity of BCFO was also measured as a function of time under air at 550 °C, as shown in Fig. 13. After long-term operation for 115 h, the change in the conductivity of BCFO was negligible, indicating the robustness and stability of the BCFO. That is, the BCFO showed promise for SOFCs as a cathode material.

4. Conclusions

We explored, for the first time, the use of bismuth ferrite (BFO)-based materials as a novel cobalt-free oxygen electrode catalyst at both low and high temperatures. Among these, CaO-doped BFO (BCFO) showed good catalytic activity and high stability for OER and ORR in URFCs and SOFCs. The onset and half-wave potentials at −3 mA cm^{-2} of BCFO were 0.705 and 0.619 V, respectively for ORR, while those of BFO were 0.633 and 0.480 V. The measured Tafel slopes of BFO and BCFO catalysts were −99

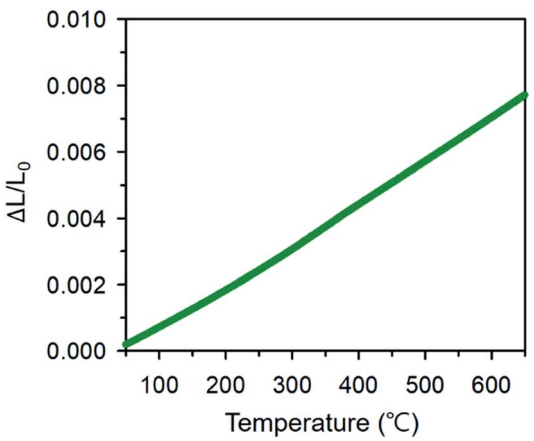

Fig. 11 Thermal expansion coefficient of BCFO at between room temperature and 650 °C.

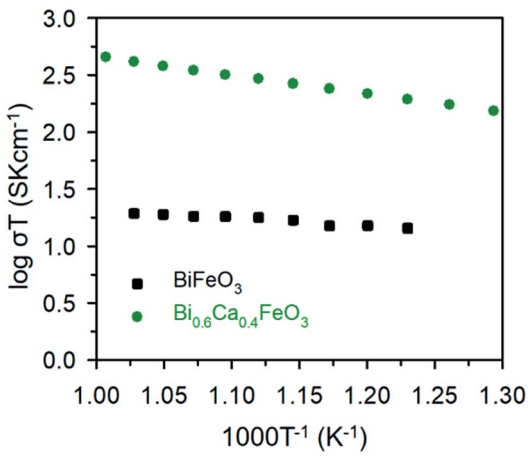

Fig. 12 DC conductivity of BFO and BCFO as a function of temperature.

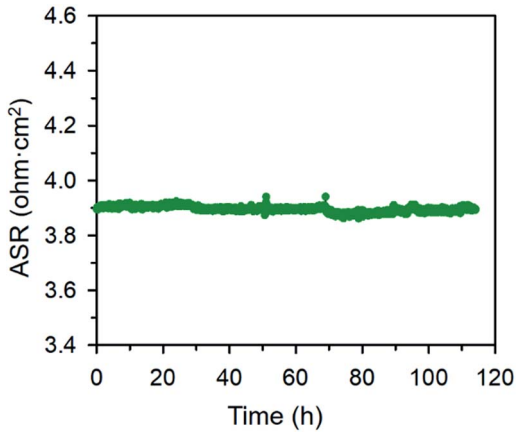

Fig. 13 Area specific resistances of the BCFO as a function of time at 650 °C for the stability test.

and −76 mV dec^{-1}, respectively, for ORR. The current density for OER of BCFO showed a significantly high value of 6.93 mA cm^{-2}, at a fixed overpotential of 0.42 V (1.65 V *vs.* RHE), which was approximately 2 times higher than that of other BFO-based catalysts. The excellent performance of BCFO for OER and ORR was because the doping of CaO into BFO resulted in the increment of the transport rates of charge species for the electrochemical reactions through the change of electronic structure, which was confirmed by EIS measurements. BCFO also recorded outstandingly lesser performance decay ratios after the cycling tests for OER and ORR than that of the pristine BFO in an alkaline medium. For further improvement of the activity and stability, BFO-based electrocatalyst would be hybridized with the nitrogen doped reduced graphene oxide, heteroatom doped carbon nanotubes (or carbon nanofiber), and conducting polymeric materials (such as polyaniline) as future works. We also investigated the electrical conductivity of BCFO at elevated temperatures, and BCFO exhibited 2–3 orders higher values at 500−700 °C than did BFO. In summary, the feasibility of BCFO was demonstrated as the oxygen electrode material for ORR and OER at both room temperature and elevated temperatures.

Conflicts of interest

There are no conflicts to declare.

Acknowledgements

This research was supported by the Mid-career Researcher and Technology Development Program to Solve Climate Changes through the National Research Foundation of Korea (NRF-2014R1A2A1A11052276 and NRF-2015M1A2A2057042) and by the Industrial Technology Innovation and International Collaborative Energy Technology R&D Program of the Korea Institute of Energy Technology Evaluation and Planning (KETEP) granted financial resource from the Ministry of Trade, Industry & Energy, Republic of Korea (No. 20153010031940 and No. 20158520030830).

References

1 A. S. Aricò, P. Bruce, B. Scrosati, J.-M. Tarascon and W. van Schalkwijk, *Nat. Mater.*, 2005, **4**, 366.
2 S. Park, Y. Shao, J. Liu and Y. Wang, *Energy Environ. Sci.*, 2012, **5**, 9331.
3 J. C. Burns, A. Kassam, N. N. Sinha, L. E. Downie, L. Solnickova, B. M. Way and J. R. Dahn, *J. Electrochem. Soc.*, 2013, **160**, A1451.
4 G. Wang, L. Zhang and J. Zhang, *Chem. Soc. Rev.*, 2012, **41**, 797.
5 O. Gröger, H. A. Gasteiger and J.-P. Suchsland, *J. Electrochem. Soc.*, 2015, **162**, A2605.
6 E. D. Wachsman and K. T. Lee, *Science*, 2011, **334**, 935.
7 B. C. H. Steele and A. Heinzel, *Nature*, 2001, **414**, 345.
8 V. Ramani, *Electrochem. Soc. Interface*, 2006, **15**, 41.
9 L. Carrette, K. A. Friedrich and U. Stimming, *ChemPhysChem*, 2000, **1**, 162.
10 A. Brisse, J. Schefold and M. Zahid, *Int. J. Hydrogen Energy*, 2008, **33**, 5375.
11 F. Mitlitsky, B. Myers and A. H. Weisberg, *Energy Fuels*, 1998, **12**, 56.
12 S.-D. Yim, W. Y. Lee, Y.-G. Yoon, Y.-J. Sohn, G.-G. Park, T.-H. Yang and C.-S. Kim, *Electrochim. Acta*, 2004, **50**, 713.
13 G. Chen, S. R. Bare and T. E. Mallouk, *J. Electrochem. Soc.*, 2002, **149**, A1092.
14 J. Pettersson, B. Ramsey and D. Harrison, *J. Power Sources*, 2006, **157**, 28.
15 M. A. Laguna-Bercero, *J. Power Sources*, 2012, **203**, 4.
16 M.-B. Choi, B. Singh, E. D. Wachsman and S.-J. Song, *J. Power Sources*, 2013, **239**, 361.
17 Y. Gorlin and T. F. Jaramillo, *J. Am. Chem. Soc.*, 2010, **132**, 13612.
18 B. Hua, Y.-Q. Zhang, N. Yan, M. Li, Y.-F. Sun, J. Chen, J. Li and J.-L. Luo, *Adv. Funct. Mater.*, 2016, **26**, 4106.
19 W. T. Hong, M. Risch, K. A. Stoerzinger, A. Grimaud, J. Suntivich and Y. Shao-Horn, *Energy Environ. Sci.*, 2015, **8**, 1404.
20 D. N. Leonard, A. Kumar, S. Jesse, M. D. Biegalski, H. M. Christen, E. Mutoro, E. J. Crumlin, Y. Shao-Horn, S. V. Kalinin and A. Y. Borisevich, *Adv. Energy Mater.*, 2013, **3**, 788.
21 N.-I. Kim, Y. J. Sa, S.-H. Cho, I. So, K. Kwon, S. H. Joo and J.-Y. Park, *J. Electrochem. Soc.*, 2016, **163**, F3020.
22 M. Jiang, Y. Li, X. Sun and X. Duan, *Inorg. Chem. Front.*, 2016, **3**, 630.
23 T. Y. Ma, J. Ran, S. Dai, M. Jaroniec and S. Z. Qiao, *Angew. Chem., Int. Ed.*, 2015, **54**, 4646.
24 R. Cao, J.-S. Lee, M. Liu and J. Cho, *Adv. Energy Mater.*, 2012, **2**, 816.
25 J. Suntivich, H. A. Gasteiger, N. Yabuuchi, H. Nakanishi, J. B. Goodenough and Y. Shao-Horn, *Nat. Chem.*, 2011, **3**, 546.
26 J. Suntivich, K. J. May, H. A. Gasteiger, J. B. Goodenough and Y. Shao-Horn, *Science*, 2011, **334**, 1383.

27 A. Grimaud, K. J. May, C. E. Carlton, Y.-L. Lee, M. Risch, W. T. Hong, J. Zhou and Y. Shao-Horn, *Nat. Commun.*, 2013, **4**, 2439.
28 W. Zhou, J. Sunarso, Z.-G. Chen, L. Ge, J. Motuzas, J. Zou, G. Wang, A. Julbe and Z. Zhu, *Energy Environ. Sci.*, 2011, **4**, 872.
29 C. P. Jijil, M. Lokanathan, S. Chithiravel, C. Nayak, D. Bhattacharyya, S. N. Jha, P. D. Babu, B. Kakade and R. N. Devi, *ACS Appl. Mater. Interfaces*, 2016, **8**, 34387.
30 C. P. Jijil, S. M. Unni, K. Sreekumar and R. N. Devi, *Chem. Mater.*, 2012, **24**, 2823.
31 S. Choi, S. Yoo, J. Kim, S. Park, A. Jun, S. Sengodan, J. Kim, J. Shin, H. Y. Jeong, Y. Choi, G. Kim and M. Liu, *Sci. Rep.*, 2013, **3**, 2426.
32 Z. Shao and S. M. Haile, *Nature*, 2004, **431**, 170.
33 D. J. K. Brett, A. Atkinson, N. P. Brandon and S. J. Skinner, *Chem. Soc. Rev.*, 2008, **37**, 1568.
34 T.-H. Lee, S.-S. Baek, K.-Y. Park, Y. Seo, B. Park, H.-T. Lim and J.-Y. Park, *J. Alloys Compd.*, 2017, **706**, 330.
35 K.-Y. Park, T.-H. Lee, S. Jo, J. Yang, S.-J. Song, H.-T. Lim, J. H. Kim and J.-Y. Park, *J. Power Sources*, 2016, **336**, 437.
36 C. Jeong, H.-H. Lee, M. Park, J. Hong, H. Kim, J.-W. Son, J.-H. Lee, B.-K. Kim and K. J. Yoon, *J. Power Sources*, 2015, **297**, 370.
37 W. Zhou, R. Ran and Z. Shao, *J. Power Sources*, 2009, **192**, 231.
38 R. Zeng and Y. Huang, *Int. J. Hydrogen Energy*, 2017, **42**, 7220.
39 T.-H. Lee, K.-Y. Park, N.-I. Kim, S.-J. Song, K.-H. Hong, D. Ahn, A. K. Azad, J. Hwang, S. Bhattacharjee, S.-C. Lee, H.-T. Lim and J.-Y. Park, *J. Power Sources*, 2016, **331**, 495.
40 T. Hong, M. Zhao, K. Brinkman, F. Chen and C. Xia, *ACS Appl. Mater. Interfaces*, 2017, **9**, 8659.
41 B. Wei, Z. Lü, X. Huang, M. Liu, N. Li and W. Su, *J. Power Sources*, 2008, **176**, 1.
42 Q. Zhou, W. Wang, T. Wei, X. Qi, Y. Li, Y. Zou, Y. Liu, Z. Li and Y. Wu, *Ceram. Int.*, 2012, **38**, 1529.
43 Y. Niu, W. Zhou, J. Sunarso, F. Liang, Z. Zhu and Z. Shao, *Electrochem. Commun.*, 2011, **13**, 1340.
44 H. J. Park and J. Y. Park, *Solid State Ionics*, 2013, **244**, 30.
45 J. Richter, P. Holtappels, T. Graule, T. Nakamura and L. J. Gauckler, *Monatsh. Chem.*, 2009, **140**, 985.
46 Y.-C. Tu, C.-Y. Chang, M.-C. Wu, J.-J. Shyue and W.-F. Su, *RSC Adv.*, 2014, **4**, 19925.
47 I. Papadas, J. A. Christodoulides, G. Kioseoglou and G. S. Armatas, *J. Mater. Chem. A*, 2015, **3**, 1587.
48 W. Liu, G. Tan, X. Xue, G. Dong and H. Ren, *J. Mater. Sci.: Mater. Electron.*, 2013, **24**, 4827.
49 M. Tokunaga, M. Akaki, T. Ito, S. Miyahara, A. Miyake, H. Kuwahara and N. Furukawa, *Nat. Commun.*, 2015, **6**, 5878.
50 G. Kim, N. Lee, K. B. Kim, B. K. Kim, H. Chang, S. J. Song and J. Y. Park, *Int. J. Hydrogen Energy*, 2013, **38**, 1571.
51 N.-I. Kim, R. A. Afzal, S. R. Choi, S. W. Lee, D. Ahn, S. Bhattacharjee, S.-C. Lee, J. H. Kim and J.-Y. Park, *J. Mater. Chem. A*, 2017, **5**, 13019.
52 P. Kumar, C. Panda and M. Kar, *Smart Mater. Struct.*, 2015, **24**, 045028.
53 N. Ramadass, *Mater. Sci. Eng.*, 1978, **36**, 231.
54 B. Bhushan, A. Basumallick, S. K. Bandopadhyay, N. Y. Vasanthacharya and D. Das, *J. Phys. D: Appl. Phys.*, 2009, **42**, 065004.
55 M. Hasan, M. A. Basith, M. A. Zubair, M. S. Hossain, R. Mahbub, M. A. Hakim and M. F. Islam, *J. Alloys Compd.*, 2016, **687**, 701.
56 U. A. Paulus, A. Wokaun, G. G. Scherer, T. J. Schmidt, V. Stamenkovic, V. Radmilovic, N. M. Markovic and P. N. Ross, *J. Phys. Chem. B*, 2002, **106**, 4181.
57 Y. Feng and N. Alonso-Vante, *Electrochim. Acta*, 2012, **72**, 129.
58 Y. Li, Z. W. Wang, C.-Y. Chiu, L. Ruan, W. Yang, Y. Yang, R. E. Palmer and Y. Huang, *Nanoscale*, 2012, **4**, 845.
59 Y. Liang, Y. Li, H. Wang, J. Zhou, J. Wang, T. Regier and H. Dai, *Nat. Mater.*, 2011, **10**, 780.
60 S. Han and C. S. Kim, *J. Appl. Phys.*, 2013, **113**, 17D921.
61 Z. Quan, H. Hu, S. Xu, W. Liu, G. Fang, M. Li and X. Zhao, *J. Sol-Gel Sci. Technol.*, 2008, **48**, 261.
62 A. P. Grosvenor, B. A. Kobe, M. C. Biesinger and N. S. McIntyre, *Surf. Interface Anal.*, 2004, **36**, 1564.
63 T. Susi, T. Pichler and P. Ayala, *Beilstein J. Nanotechnol.*, 2015, **6**, 177.
64 T. Saitoh, A. E. Bocquet, T. Mizokawa, H. Namatame and A. Fujimori, *Phys. Rev. B: Condens. Matter Mater. Phys.*, 1995, **51**, 13942.
65 A. L. Gal and S. Abanades, *J. Phys. Chem. C*, 2012, **116**, 13516.
66 S.-T. Myung, A. Ogata, K.-S. Lee, S. Komaba, Y.-K. Sun and H. Yashiro, *J. Electrochem. Soc.*, 2008, **155**, A374.
67 R. Hausbrand, G. Cherkashinin, H. Ehrenberg, M. Gröting, K. Alba, C. Hess and W. Jaegermann, *Mater. Sci. Eng., B*, 2015, **192**, 3.
68 I.-S. So, N.-I. Kim, S.-H. Cho, Y.-R. Kim, J. Yoo, Y. Seo, Y.-S. Seo, B. Park, K. Kwon and J.-Y. Park, *J. Electrochem. Soc.*, 2016, **163**, F3041.
69 K. J. May, C. E. Carlton, K. A. Stoerzinger, M. Risch, J. Suntivich, Y.-L. Lee, A. Grimaud and Y. Shao-Horn, *J. Phys. Chem. Lett.*, 2012, **3**, 3264.
70 A. Grimaud, C. E. Carlton, M. Risch, W. T. Hong, K. J. May and Y. Shao-Horn, *J. Phys. Chem. C*, 2013, **117**, 25926.
71 A. Bergmann, E. Martinez-Moreno, D. Teschner, P. Chernev, M. Gliech, J. F. de Araújo, T. Reier, H. Dau and P. Strasser, *Nat. Commun.*, 2015, **6**, 8625.
72 J.-H. Kim and A. Manthiram, *J. Electrochem. Soc.*, 2008, **155**, B385.
73 J. C. Ruiz-Morales, D. Marrero-López, J. Canales-Vázquez and J. T. S. Irvine, *RSC Adv.*, 2011, **1**, 1403.
74 K. T. Lee and A. Manthiram, *J. Electrochem. Soc.*, 2006, **153**, A794.
75 J. H. Kim and J. T. S. Irvine, *Int. J. Hydrogen Energy*, 2012, **37**, 5920.
76 L. Zhao, J. Shen, B. He, F. Chen and C. Xia, *Int. J. Hydrogen Energy*, 2011, **36**, 3658.
77 Y. Huang, K. Ahn, J. M. Vohs and R. J. Gorte, *J. Electrochem. Soc.*, 2004, **151**, A1592.
78 G. Kim, N. Lee, K.-B. Kim, B.-K. Kim, H. Chang, S.-J. Song and J.-Y. Park, *Int. J. Hydrogen Energy*, 2013, **38**, 1571.
79 C. Kwak, D. W. Jung, D.-H. Yeon, J. S. Kim, H. J. Park, S.-J. Ahn, S. Seo and S. M. Lee, *RSC Adv.*, 2013, **3**, 10669.